

See discussions, stats, and author profiles for this publication at: <https://www.researchgate.net/publication/6567770>

Water Solubility in Aluminous Orthopyroxene and the Origin of Earth's Asthenosphere

Article in Science · February 2007

DOI: 10.1126/science.1135422 · Source: PubMed

CITATIONS

293

READS

788

4 authors, including:



Joseph R Smyth

University of Colorado Boulder

277 PUBLICATIONS 8,335 CITATIONS

SEE PROFILE



Falko Langenhorst

Institut für Geowissenschaften

378 PUBLICATIONS 12,583 CITATIONS

SEE PROFILE



Water Solubility in Aluminous Orthopyroxene and the Origin of Earth's Asthenosphere

Katrin Mierdel, *et al.*

Science **315**, 364 (2007);

DOI: 10.1126/science.1135422

The following resources related to this article are available online at www.sciencemag.org (this information is current as of January 22, 2007):

Updated information and services, including high-resolution figures, can be found in the online version of this article at:

<http://www.sciencemag.org/cgi/content/full/315/5810/364>

Supporting Online Material can be found at:

<http://www.sciencemag.org/cgi/content/full/315/5810/364/DC1>

A list of selected additional articles on the Science Web sites **related to this article** can be found at:

<http://www.sciencemag.org/cgi/content/full/315/5810/364#related-content>

This article **cites 17 articles**, 5 of which can be accessed for free:

<http://www.sciencemag.org/cgi/content/full/315/5810/364#otherarticles>

This article appears in the following **subject collections**:

Geochemistry, Geophysics

http://www.sciencemag.org/cgi/collection/geochem_phys

Information about obtaining **reprints** of this article or about obtaining **permission to reproduce this article** in whole or in part can be found at:

<http://www.sciencemag.org/help/about/permissions.dtl>

release from litter high in initial N. The TNET was at least 50% faster for most leaf litters decomposed in temperate deciduous forests when compared to coniferous forests and humid grasslands, all with similar CDIs (Table 1). Within a given CDI level, other factors such as edaphic conditions or decomposer communities may contribute to the differences observed (29, 30). At the highest leaf litter N concentrations, all biomes experienced net N release during the first year of decomposition.

Root litter N followed a linear pattern with mass remaining (Fig. 3) and could best be described by two equations. The first was for *D. glauca* roots, which demonstrated a small amount of net N immobilization early in decomposition for a range of sites, possibly due to slightly higher concentrations of nonpolar extractives and slightly lower acid extractable carbohydrates concentrations than the other species (table S2). The second equation described net N release for the pine and grass roots that did not immobilize N during decomposition. A comparison of litter N dynamics during decomposition of pine and grass roots with leaf litter of similar initial N concentration (Figs. 2 and 3) showed that N was released from roots much more rapidly than from leaf litter. Roots released N as soon as litter decomposition was initiated (C:N ratio > 50). Microbial decomposers in the soil may have greater access to moisture, organic matter, and mineral N than microbes involved in leaf litter decomposition at the soil surface, which would facilitate net N release during decomposition (31). Similar patterns in net N release in roots have been described for native root litter decomposed in situ in grasslands (32), temperate broadleaf forests (33), temperate conifer forests (34), and moist and humid tropical forests (35, 36).

Our data show that the initial N concentration of leaf litter is a dominant driver of net N immobilization and release during long-term litter decomposition at a global scale. This occurs regardless of climate, other litter chemical properties, edaphic conditions, or soil microbial communities. Our data also show that N can be released early in decomposition from high-quality litters in environments that support low decomposition rates. The time required to initiate net N release was predicted from the initial N of the litter and the CDI across biomes, but required more site information within a given CDI. Roots generally lost N linearly with mass loss during decomposition. Because N release during decay plays a fundamental role in net ecosystem production, improved understanding of the controls on net N release during decomposition is likely to greatly improve our ability to predict terrestrial C dynamics at global and regional scales.

References and Notes

- H. L. Gholz, D. Wedin, S. Smitherman, M. E. Harmon, W. J. Parton, *Global Change Biol.* **6**, 751 (2000).
- I. C. Prentice *et al.*, in *Climate Change 2001: The Scientific Basis: Contribution of Working Group I to the Third Assessment Report of the Intergovernmental Panel on Climate Change*, J. T. Houghton *et al.*, Eds. (Cambridge Univ. Press, Cambridge, 2001), pp. 183–231.
- B. Moore, B. H. Braswell, *Ambio* **23**, 4 (1994).
- W. S. Currie, *Global Change Biol.* **9**, 919 (2003).
- P. M. Vitousek, R. W. Howarth, *Biogeochemistry* **13**, 87 (1991).
- J. D. Lousier, D. Parkinson, *Can. J. For. Res.* **9**, 449 (1979).
- B. Berg, C. McClaugherty, *Can. J. Bot.* **67**, 1148 (1989).
- B. Berg, *For. Ecol. Manage.* **133**, 13 (2000).
- J. D. Aber, J. M. Melillo, C. A. McClaugherty, *Can. J. Bot.* **68**, 2201 (1990).
- R. Aerts, *Oikos* **79**, 439 (1997).
- G. Cadisch, K. E. Giller, Eds., *Driven by Nature: Plant Litter Quality and Decomposition* (CAB International, Oxon, UK, 1997).
- Long-Term Intersite Decomposition Experiment Team (LIDET), *Meeting the Challenges of Long-Term, Broad-Scale Ecological Experiments* (Publication No. 19, U.S. Long Term Ecological Research Network Office, Seattle, WA, 1995).
- W. M. Post, J. Pastor, *Clim. Change* **34**, 253 (1996).
- D. L. Moorhead, W. S. Currie, E. B. Rastetter, W. J. Parton, M. E. Harmon, *Global Biogeochem. Cycles* **13**, 575 (1999).
- J. Rozema *et al.*, *Plant Ecol.* **128**, 284 (1997).
- V. A. Pancotto, O. E. Sala, T. M. Robson, M. M. Caldwell, A. L. Scopel, *Global Change Biol.* **11**, 1982 (2005).
- A. T. Austin, L. Vivanco, *Nature* **442**, 555 (2006).
- Materials and methods are available as supporting material on Science Online.
- E. H. Richards, A. G. Norman, *Biochem. J.* **25**, 1769 (1931).
- J. D. Aber, J. M. Melillo, *Can. J. Bot.* **60**, 2263 (1982).
- S. E. Hobbie, P. M. Vitousek, *Ecology* **81**, 1867 (2000).
- T. R. Moore, J. A. Trofymow, C. E. Prescott, J. Fyles, B. D. Titus, *Ecosystems* **9**, 46 (2006).
- M. H. Beare *et al.*, *Ecol. Monogr.* **62**, 569 (1992).
- S. D. Frey, M. Knorr, J. L. Parrent, R. T. Simpson, *For. Ecol. Manage.* **196**, 159 (2004).
- S. D. Frey, E. T. Elliott, K. Paustian, G. A. Peterson, *Soil Biol. Biochem.* **32**, 689 (2000).
- D. S. Schimel *et al.*, *Ecology* **72**, 672 (1991).
- H. A. Verhoef, J. M. H. Verspagen, H. R. Zoomer, *Biol. Fertil. Soils* **31**, 366 (2000).
- S. A. Moody *et al.*, *Plant Ecol.* **154**, 27 (2001).
- J. D. Aber, J. M. Melillo, K. J. Nadelhoffer, C. A. McClaugherty, J. Pastor, *Oecologia* **66**, 317 (1985).
- J. E. Barrett, R. L. McCulley, D. R. Lane, I. C. Burke, W. K. Lauenroth, *J. Veg. Sci.* **13**, 383 (2002).
- W. L. Silver, R. K. Miya, *Oecologia* **129**, 407 (2001).
- T. R. Seastedt, W. J. Parton, D. S. Ojima, *Can. J. Bot.* **70**, 384 (1992).
- M. E. Dornbush, T. M. Isenhardt, J. W. Raich, *Ecology* **83**, 2985 (2002).
- H. Chen, M. E. Harmon, J. Sexton, B. Fasth, *Can. J. For. Res.* **32**, 320 (2002).
- W. L. Silver, K. A. Vogt, *J. Ecol.* **8**, 729 (1993).
- W. L. Silver *et al.*, *Global Change Biol.* **11**, 290 (2005).
- W. J. Parton, D. S. Schimel, D. S. Ojima, C. V. Cole, in *Quantitative Modeling of Soil Formation Processes*, R. B. Bryant, R. W. Arnold, Eds. (SSSA Special Publication 39 ASA, CSSA, and SSSA, Madison, WI, 1994), pp. 147–167.
- The LIDET study was supported by NSF Ecosystems Studies grants BSR-8805390 and BSR-9180329 to Oregon State University, NSF Shortgrass Steppe LTER grant DEB-350273, NSF IRC grant DEB-9977066, and University of Tennessee–Battelle, LLC (U.S. Department of Energy) subcontract grant 4000050162. This work was conducted as part of the Long-Term Intersite Decomposition Working Group supported by the National Center for Ecological Analysis and Synthesis, a Center funded by NSF (grant DEB-0072909), University of California, Santa Barbara. W.S. was also supported by NSF grants DEB-0218039, DEB-0219104, and the California Agricultural Experiment Station (7069-MS). W.P. was supported by DOE ORNL grant 533906, NSF grant DEB-0217631, and the NSF UV radiation project at the University of Minnesota. We thank H. Gholz for invaluable input on previous versions of this manuscript, and S. Lutz, C. Keough, and L. Richards for assistance in analyzing the extensive LIDET litter decay data set.

Supporting Online Material

www.sciencemag.org/cgi/content/full/315/5810/361/DC1
Materials and Methods
Tables S1 to S3
References

7 September 2006; accepted 5 December 2006
10.1126/science.1134853

Water Solubility in Aluminous Orthopyroxene and the Origin of Earth's Asthenosphere

Katrin Mierdel,¹ Hans Keppler,^{1,2*} Joseph R. Smyth,^{2,3} Falko Langenhorst^{2,4}

Plate tectonics is based on the concept of rigid lithosphere plates sliding on a mechanically weak asthenosphere. Many models assume that the weakness of the asthenosphere is related to the presence of small amounts of hydrous melts. However, the mechanism that may cause melting in the asthenosphere is not well understood. We show that the asthenosphere coincides with a zone where the water solubility in mantle minerals has a pronounced minimum. The minimum is due to a sharp decrease of water solubility in aluminous orthopyroxene with depth, whereas the water solubility in olivine continuously increases with pressure. Melting in the asthenosphere may therefore be related not to volatile enrichment but to a minimum in water solubility, which causes excess water to form a hydrous silicate melt.

Earth's asthenosphere is often assumed to roughly coincide with the low-velocity zone, a layer of reduced seismic velocities and increased attenuation of seismic waves. The low-velocity zone usually begins at a depth

of 60 to 80 km below the oceans and ends around 220 km (*1*). Below continental shields, the upper boundary is depressed to 150 km. The seismic characteristics of the low-velocity zone could be easily explained by the presence of a small frac-

Table 1. Experimental results on water solubility in aluminum-saturated enstatite. All experiments were carried out using an oxide-hydroxide mixture as starting material, except as noted. Number of infrared measurements refers to the numbers of different spots measured, usually on different crystals. Water contents (in ppm by weight) were calculated from the infrared data according to two different extinction coefficients, from Bell *et al.* (13) and from Paterson (28). Errors are one standard deviation. Water contents in atoms H per 10^6 Si can be obtained by multiplying by a factor of 22.3. All data reported here for a given pressure and temperature were included in the calibration of the thermodynamic model of water solubility. Solid phases detected refer to those phases that could be directly observed by x-ray diffraction or Raman spectroscopy. However, all the samples must have contained some aluminous phase, probably spinel or pyrope, as the

aluminum content of the orthopyroxene was always several weight % lower than the aluminum content of the starting material. A fluid phase was always present during the experiments, as all samples released considerable amounts of water upon opening of the capsules. No evidence for melting was seen, as the run products were usually loose powders without interstitial glass. Some fluffy material and isolated glass beads probably represent material precipitated from the fluid upon quenching. En, enstatite; Sp, spinel; Ol, olivine; Prp, pyrope; Crn, corundum; Ky, kyanite; Sr, sapphirine; Prl, pyrophyllite. Al contents in enstatite were sometimes slightly inhomogeneous. The numbers and standard deviations given were usually derived from more than 100 individual analyses of different crystals in the charge. The molar Mg/Si ratio in all samples is equal to 1 within the error of the measurement.

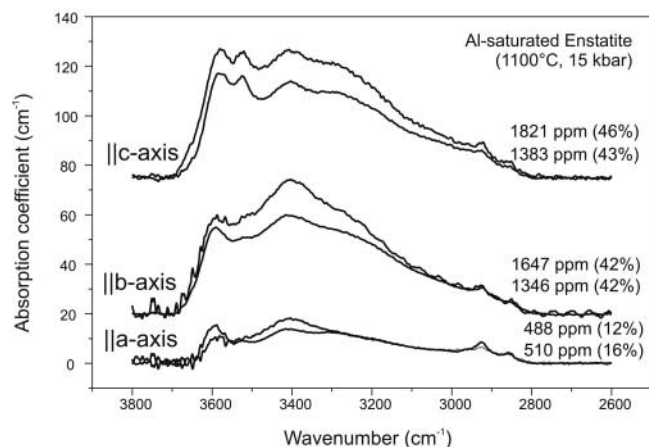
Sample	T (°C)	P (kbar)	Duration (hours)	Number of infrared measurements	Water content (ppm)		Solid phases detected	Al ₂ O ₃ content in enstatite (weight %)
					Bell <i>et al.</i> (13)	Paterson (28)		
En63	800	15	168	2	8420 ± 750	6280 ± 235	En, Crn	9.2 ± 0.99
En59/4	900	15	70	6	3710 ± 795	2810 ± 575	En, Ol, Sp, Sr	10.05 ± 0.85
En59/1	900	15	168	5	8380 ± 3030	6730 ± 2280	En, Crn	8.99 ± 1.5
En59	900	15	168	14	8290 ± 2650	6720 ± 2210	En, Crn	11.9 ± 2.22
En60	1000	15	120	6	3110 ± 600	2440 ± 465	En	8.28 ± 2.2
En47*	1100	15	120	5	2460 ± 960	1860 ± 780	En, Ol, Sp	6.7 ± 1.33
En47/1	1100	15	120	4	1730 ± 450	1340 ± 325	En	8.77 ± 2.16
En47/2	1100	15	168	2	1590 ± 185	1290 ± 255	En, Sp, (Ol)	8.96 ± 1.46
En86	800	25	168	2	4670 ± 655	3590 ± 600	En, Ky	6.67 ± 2.44
En85	900	25	168	4	6400 ± 1330	5040 ± 885	En	5.57 ± 1.56
En84	1100	25	120	2	1420 ± 115	1080 ± 190	En, Ol	5.4 ± 0.84
En87*	1000	35	120	2	1680 ± 490	1140 ± 340	En, Prp	1.73 ± 0.21
En87/2	1000	35	120	6	2370 ± 450	1640 ± 435	En, Ol, Prp	1.21 ± 0.61
En70*	1100	35	168	1	1230	960	En, Ol, Prp	1.75 ± 0.65
En90/1	1100	35	120	3	1500 ± 305	1150 ± 280	En, Ol, Prp, Prl	1.57 ± 0.25

*Synthesized from gels.

tion of partial melt as intergranular film (1, 2). Some water is required to generate such a partial melt in the mantle, as mantle temperatures at the relevant depths are below the dry melting point of peridotite but above the water-saturated solidus (3, 4). Originally, it was believed that the top of the low-velocity zone corresponds to the stability limit of hydrous phases such as phlogopite or hornblende (5, 6). However, this is unlikely because the solubility of water (and of alkalis) in nominally anhydrous mantle minerals (7–9) is so high that separate hydrous phases such as amphiboles and phlogopite are not stable in an upper mantle of pyrolytic composition.

If the low-velocity zone were due to partial melting, the existence of a lower boundary would be even more difficult to understand, as the geotherm remains above the water-saturated solidus with increasing depth. Moreover, it is unclear whether low degrees of partial melt in the mantle would form an intergranular film (10), as dry

Fig. 1. Polarized infrared spectra of two aluminum-saturated enstatite crystals synthesized at 1100°C and 15 kbar. Water contents (in ppm) correspond to the absorbances measured parallel to the three crystallographic axes. Bulk water contents are obtained by adding these values. Numbers in parentheses denote percentage of total water observed in each of the three directions of polarization. The spectra shown here and in Fig. 2 were obtained from the raw data by subtracting a linear baseline defined by the points at 3800 cm^{-1} and 2800 cm^{-1} . The two weak features between 2800 cm^{-1} and 3000 cm^{-1} could be due to organic surface contamination. However, they persisted after repolishing and they may therefore be intrinsic to the sample.



basaltic melts do not wet mantle minerals and therefore tend to form isolated pockets. Accordingly, alternative models have been proposed. These models (10, 11) are based on the observation that water dissolved in mantle minerals such as olivine reduces both the strength of the mineral and the seismic velocities. The boundary between lithosphere and asthenosphere may then correspond to a boundary in intracrystalline water content, with the asthenosphere

being water-rich, whereas the oceanic lithosphere is depleted in water as a result of the melt extraction at mid-ocean ridges. The presence of partial melt in the asthenosphere is not required in these models. However, they cannot explain the existence of a low-velocity zone below continental shields, as the mechanism of magma production below continents is very different from that prevailing at mid-ocean ridges.

¹Institut für Geowissenschaften, Universität Tübingen, Wilhelmstr. 56, 72074 Tübingen, Germany. ²Bayerisches Geoinstitut, Universität Bayreuth, 95440 Bayreuth, Germany. ³Department of Geological Sciences, University of Colorado, Boulder, CO 80309, USA. ⁴Institut für Geowissenschaften, Friedrich-Schiller-Universität Jena, Burgweg 11, 07749 Jena, Germany.

*To whom correspondence should be addressed. E-mail: hans.keppeler@uni-bayreuth.de

All models of the low-velocity zone depend on the presence of water and its solubility in mantle minerals. The main constituents of the upper mantle are olivine and orthopyroxene (enstatite). The water solubility in both olivine and Al-free orthopyroxene is quite comparable and increases with pressure and temperature (7–9, 12). However, aluminum is known to greatly enhance water solubility in orthopyroxene, and at high Al contents, water in orthopyroxene may dominate the water budget in the mantle. Throughout Earth's upper mantle, olivine and orthopyroxene usually coexist with small amounts of an aluminous phase such as spinel or garnet. Therefore, we experimentally studied the solubility of water in aluminous MgSiO_3 enstatite in equilibrium with spinel or garnet (i.e., under conditions of aluminum saturation).

Experiments were carried out in an end-loaded piston-cylinder apparatus. Mixtures of $\text{Mg}(\text{OH})_2$, $\text{Al}(\text{OH})_3$, and SiO_2 were sealed in platinum-rhodium ($\text{Pt}_{0.95}\text{Rh}_{0.05}$) capsules together with about 20 weight % of liquid water. The stoichiometry of the starting mixture was chosen to correspond to aluminous orthopyroxene plus small amounts of olivine and spinel or garnet. In some experiments, homogeneous mixtures of the starting chemicals were used. In most experiments, however, alternating layers with low and high silica content were introduced into the capsule to reduce nucleation rates so as to grow larger crystals. In addition, some experiments were carried out with amorphous gels and liquid water as starting material. Experiments were run at 15 to 35 kbar and 800° to 1100°C for a few days. After the experiments, the capsules were opened. Capsules that did not release excess water after the experiment were discarded. Perfectly clear and inclusion-free single crystals of orthopyroxene were picked from the charges, optically oriented, and doubly polished. Polarized infrared spectra (Fig. 1) were measured with a Bruker IFS 125 Fourier-transform infrared spectrometer coupled with an IRscope I microscope (tungsten source, CaF_2 beam splitter, narrow-band mercury cadmium telluride detector, Al strip polarizer on KRS 5 substrate). Water contents were calculated from the infrared data with the use of the extinction coefficients of Bell *et al.* (13). Chemical analyses were carried out with a JEOL 8900 RL electron microprobe (15 kV, 15 nA, 120 s counting time per spot, focused beam).

The water contents in the aluminous pyroxenes are strikingly high, reaching values close to 1 weight % at low pressures and temperatures (Table 1 and Fig. 2). Water solubilities clearly decrease with both pressure and temperature, opposite to the behavior observed for olivine and Al-free enstatite. The high water solubilities are correlated with anomalously high Al contents in the pyroxenes, which are much higher than those predicted from existing thermodynamic models and experimental calibrations (14–16). However, in previous studies, only a

few experiments were carried out at the low pressures and temperatures where we observe high Al and water contents, and the water fugacity was probably not carefully controlled in all experiments. The high water contents appear to be intrinsic to the pyroxenes. The presence of foreign phases in the crystals is unlikely, because the infrared bands are strongly polarized (Fig. 1) and measurements were taken only on perfectly clear and optically inclusion-free crystals. To rule out any impurities at the submicroscopic level, we investigated several orthopyroxene crystals by transmission electron

microscopy. The structure of the pyroxene crystals (Fig. 3) is undisturbed without any foreign phases or linear and planar defects. The high water contents are therefore definitively due to OH point defects in the structure.

Electron microprobe analyses suggest that most of the water is dissolved by the coupled substitution of $\text{Al}^{3+} + \text{H}^+$ for Si^{4+} and by the substitution of $\text{Al}^{3+} + \text{H}^+$ for 2Mg^{2+} . Both substitutions appear to occur with roughly equal abundance; that is, Al is distributed about equally among tetrahedral and octahedral sites, irrespective of water content. Both substitution

Fig. 2. Polarized infrared spectra (electrical field vector E parallel to the crystallographic c axis) and total water contents of aluminum-saturated enstatite at 800° to 1100°C and 15 to 35 kbar. Numbers are average water contents derived from the bulk water contents of all samples synthesized at a given pressure and temperature; n is the number of measurements. Bulk water contents were calculated as explained in Fig. 1. The water content of the sample synthesized at 25 kbar and 800°C, where only two crystals could be measured, is probably somewhat below the real water solubility under these conditions.

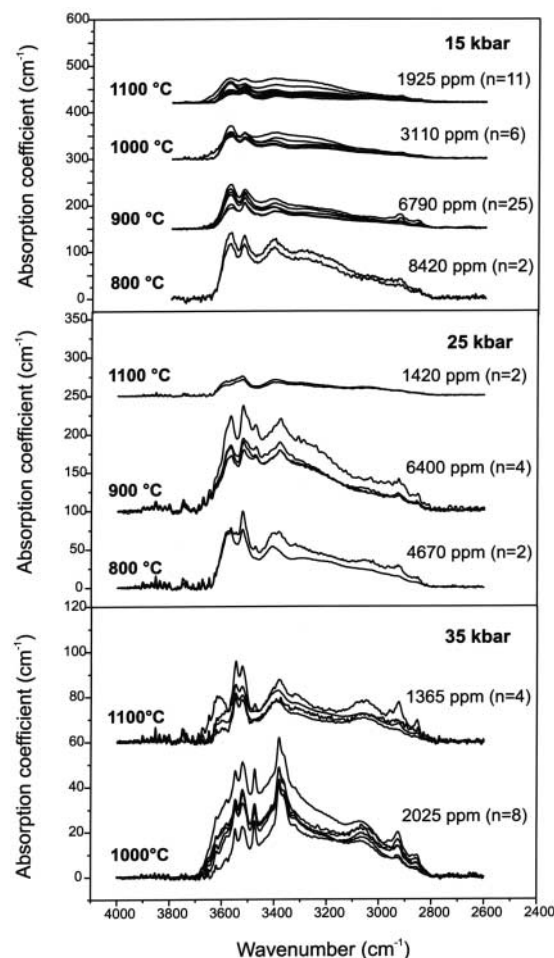
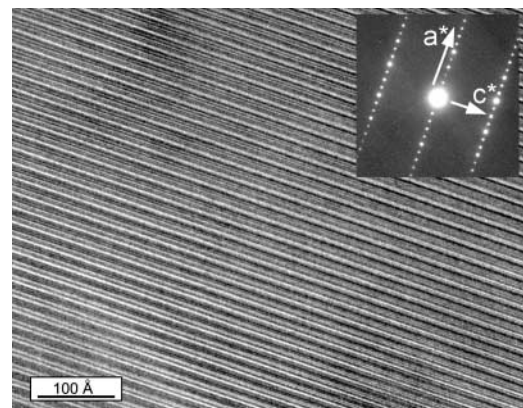


Fig. 3. Representative high-resolution transmission electron microscopy image taken along the [010] direction and corresponding selected area electron diffraction pattern (inset; a^* and c^* axes are shown) of an aluminum-saturated enstatite with 0.75 weight % water. The sample was synthesized at 15 kbar and 900°C. No evidence for foreign phases or planar defects can be detected in this image.



mechanisms imply a molar 1:1 ratio between Al and H. This is consistent with the observation that the “excess” of aluminum in the orthopyroxenes relative to existing calibrations (14–16) roughly equals the water content, if both Al_2O_3 and H_2O are expressed in molar fractions. The substitution mechanism was confirmed by a single-crystal x-ray diffraction structure refinement of one aluminous pyroxene containing 7500 ppm (by weight) of water. The structure refinement yielded 5% vacancies on one of the Mg sites [M2 (17)], consistent with H^+ substituting for Mg^{2+} and a significantly enlarged polyhedral volume of one of the Si sites [Si2 (17)] of 1.6575 \AA^3 , consistent with a substitution of $\text{Al}^{3+} + \text{H}^+$ for Si^{4+} . Structurally, the decrease in H and Al contents with increasing pressure results from the pressure destabilization of tetrahedral Al.

The systematic variations in water content with pressure and temperature observed in this study (Fig. 2) suggest that the water contents represent true equilibrium solubility. This is also supported by the observation that runs with different starting materials (oxide mixture and gels) yield similar results. To describe the water solubility in orthopyroxene coexisting with olivine and an aluminous phase as a function of pressure, temperature, and water fugacity, we calibrated a model that describes the water solubility in aluminous enstatite as the sum of the water solubility in Al-free enstatite and the water solubility coupled to aluminum. The water solubility in Al-free enstatite was previously calibrated (8, 9) and can be expressed as

$$c_{\text{water}} = A f_{\text{H}_2\text{O}} \exp\left(\frac{-\Delta H^{\text{1bar}}}{RT}\right) \exp\left(\frac{-\Delta V^{\text{solid}P}}{RT}\right) \quad (1)$$

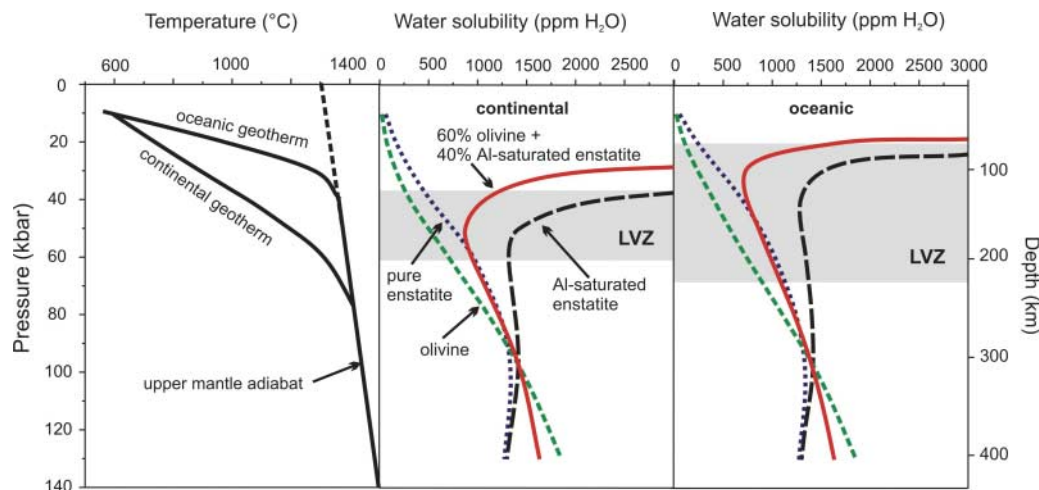
where $A = 0.01354 \text{ ppm/bar}$, $f_{\text{H}_2\text{O}}$ is water fugacity [calculated using the equation of state of (18)], $\Delta H^{\text{1bar}} = -4563 \text{ J/mol}$, $\Delta V^{\text{solid}} = 12.1 \text{ cm}^3/\text{mol}$, R is the gas constant, P is pressure, and T is absolute temperature. The additional water solubility due to Al can then be described by

$$c_{\text{water}}^{\text{Al}} = A^{\text{Al}} (f_{\text{H}_2\text{O}})^{1/2} \exp\left(\frac{-\Delta H_{\text{Al}}^{\text{1bar}}}{RT}\right) \exp\left(\frac{-\Delta V_{\text{Al}}^{\text{solid}P}}{RT}\right) \quad (2)$$

Note, however, that in Eq. 2 water fugacity enters as a square-root term (19) because the coupled substitution with Al yields isolated OH groups, unlike the OH pairs that result from the substitution of 2 H^+ for Mg^{2+} in pure enstatite (8, 9). A least-squares fit of all experimental data to Eq. 2 yielded $A^{\text{Al}} = 0.042 \text{ ppm/bar}^{0.5}$, $\Delta H_{\text{Al}}^{\text{1bar}} = -79,685 \text{ J/mol}$, and $\Delta V_{\text{Al}}^{\text{solid}} = 11.3 \text{ cm}^3/\text{mol}$. The total water solubility in orthopyroxene coexisting with olivine and either spinel or pyrope can now be calculated at any pressure and temperature by adding the results from Eqs. 1 and 2. This is consistent with observations from previous studies that the water solubility coupled to Al and the water solubility in Al-free enstatite are due to different and independent defects, with the bulk water solubility being the sum of the individual defect solubilities (8, 20). Only pressure and temperature are required to calculate the equilibrium water content in the Al-saturated orthopyroxene. This is because according to the phase rule, in a four-component system ($\text{MgO-Al}_2\text{O}_3\text{-SiO}_2\text{-H}_2\text{O}$) the coexistence of four phases (orthopyroxene, olivine, aluminous phase, and fluid) only leaves two degrees of freedom. Therefore, if pressure and temperature are given, all compositional variables in the system are determined.

Bulk mantle water solubility has a pronounced minimum (Fig. 4) between 150 and 200 km depth, coinciding with the location of the seismic low-velocity zone (shaded) below continental shields. The minimum is due to the sharp decrease of water solubility in aluminous orthopyroxene with temperature and also with pressure, whereas water solubility in olivine continuously increases with pressure and temperature (7, 12). As shown in Fig. 4, at a bulk water content of about 800 ppm, the mantle in the low-velocity zone would be oversaturated with water (i.e., the water activity would equal 1). However, as the geotherm at this depth is located above the water-saturated peridotite solidus (3, 4) of about 1000°C , a hydrous melt will form in the presence of sufficient amounts of water. Because the temperature of the geotherm is far above the water-saturated solidus under these conditions, a water activity around 0.1 is probably sufficient to induce melting (21). This water activity would imply that a few hundred ppm of water are sufficient to generate a small fraction of hydrous melt in the asthenosphere. Such water contents are to be expected in the upper mantle (22–24). If the same calculation is carried out for a hotter oceanic geotherm (Fig. 4, right panel), the upper boundary of the zone of minimum water solubility is lifted to a depth of only 60 to 80 km, consistent with the position of the low-velocity zone below oceans. Moreover, this behavior also provides a straightforward explanation for the seismic observation that the top of the low-velocity zone is very sharp and well defined, whereas the lower boundary is more diffuse and difficult to locate (2, 25). As the water solubility in mantle minerals sharply increases with decreasing depth, the fraction of partial melt in equilibrium with these minerals will also sharply decrease at the asthenosphere-lithosphere boundary. On the other hand, toward the lower boundary of the asthenosphere, the decrease in

Fig. 4. Water solubility (in ppm by weight) in upper-mantle minerals as a function of depth for a typical continental shield and oceanic geotherm (26). The typical position of the low-velocity zone (LVZ) below continental shields and below oceans is shaded in gray. Water solubility in olivine is according to Kohlstedt *et al.* (7). Water solubility in aluminum-saturated enstatite was calculated from Eqs. 1 and 2. Recently (27), it was suggested that the infrared extinction coefficient of water in olivine may be considerably smaller than previously thought. If this new calibration were applied, the water solubility in olivine would increase by a factor of about 2.5. This would somewhat sharpen the minimum in the bulk water solubility curves shown above and move them to higher water contents. It would not, however, change the general shape of the curves or the position of the inferred boundaries of the asthenosphere. The effect of using different experimental data for water solubility in olivine as well as the effect of changing the ratio of orthopyroxene to olivine is further discussed in (21).



melt fraction will be more gradual, reflecting the gradual increase of water solubility in olivine and orthopyroxene.

Our results therefore support the concept that the low-velocity zone may be related to partial melting (1, 2, 6). However, even in the absence of melting, the partitioning of water between olivine and orthopyroxene would strongly depend on depth. The high water solubilities in aluminous orthopyroxene at low pressure and temperature will effectively “dry out” olivine, and this may also contribute to a stiffening of the lithosphere. In any case, however, our results imply that the existence of an asthenosphere—and therefore of plate tectonics as we know it—is possible only in a planet with a water-bearing mantle.

References and Notes

- D. L. Anderson, *Theory of the Earth* (Blackwell Scientific, Boston, 1989).
- D. L. Anderson, C. Sammis, *Phys. Earth Planet. Inter.* **3**, 41 (1970).
- I. Kushiro, Y. Syono, S. Akimoto, *J. Geophys. Res.* **73**, 6023 (1968).
- T. Kawamoto, J. R. Holloway, *Science* **276**, 240 (1997).
- I. B. Lambert, P. J. Wyllie, *Nature* **219**, 1240 (1968).
- I. B. Lambert, P. J. Wyllie, *Science* **169**, 764 (1970).
- D. L. Kohlstedt, H. Keppler, D. C. Rubie, *Contrib. Mineral. Petrol.* **123**, 345 (1996).
- M. Rauch, H. Keppler, *Contrib. Mineral. Petrol.* **143**, 525 (2002).
- K. Mierdel, H. Keppler, *Contrib. Mineral. Petrol.* **148**, 305 (2004).
- S.-I. Karato, H. Jung, *Earth Planet. Sci. Lett.* **157**, 193 (1998).
- G. Hirth, D. L. Kohlstedt, *Earth Planet. Sci. Lett.* **144**, 93 (1996).
- Y.-H. Zhao, S. B. Ginsberg, D. L. Kohlstedt, *Contrib. Mineral. Petrol.* **147**, 155 (2004).
- D. R. Bell, P. D. Ihinger, G. R. Rossman, *Am. Mineral.* **80**, 465 (1995).
- P. A. Danckwerth, R. C. Newton, *Contrib. Mineral. Petrol.* **66**, 189 (1978).
- D. Perkins, T. J. B. Holland, R. C. Newton, *Contrib. Mineral. Petrol.* **78**, 99 (1981).
- T. Gasparik, *Phase Diagrams for Geoscientists: An Atlas of the Earth's Interior* (Springer-Verlag, Berlin, 2003).
- M. Cameron, J. J. Papike, *Rev. Mineral.* **7**, 5 (1980).
- K. S. Pitzer, S. M. Sterner, *J. Chem. Phys.* **101**, 3111 (1994).
- R. Lu, H. Keppler, *Contrib. Mineral. Petrol.* **129**, 35 (1997).
- R. Stalder, H. Skogby, *Eur. J. Mineral.* **14**, 1139 (2002).
- See supporting material on Science Online.
- D. R. Bell, G. R. Rossman, *Science* **255**, 1391 (1992).
- J. Ingrin, H. Skogby, *Eur. J. Mineral.* **12**, 543 (2000).
- N. Bolfan-Casanova, *Mineral. Mag.* **69**, 229 (2005).
- C. A. Rychert, K. M. Fischer, S. Rondenay, *Nature* **436**, 542 (2005).
- D. L. Turcotte, G. Schubert, *Geodynamics* (Cambridge Univ. Press, Cambridge, ed. 2, 2002).
- D. R. Bell, G. R. Rossman, J. Maldener, D. Endisch, F. Rauch, *J. Geophys. Res.* **108**, 10.1029/2001JB000679 (2003).
- M. S. Paterson, *Bull. Mineral.* **105**, 20 (1982).
- Supported by a Deutsche Forschungsgemeinschaft Leibniz award (H.K.) and by the Alexander von Humboldt Foundation and NSF grant EAR 0337611 (J.R.S.).

Supporting Online Material

www.sciencemag.org/cgi/content/full/315/5810/364/DC1
SOM Text
Figs. S1 and S2
References

21 September 2006; accepted 23 November 2006
10.1126/science.1135422

A Semi-Empirical Approach to Projecting Future Sea-Level Rise

Stefan Rahmstorf

A semi-empirical relation is presented that connects global sea-level rise to global mean surface temperature. It is proposed that, for time scales relevant to anthropogenic warming, the rate of sea-level rise is roughly proportional to the magnitude of warming above the temperatures of the pre-Industrial Age. This holds to good approximation for temperature and sea-level changes during the 20th century, with a proportionality constant of 3.4 millimeters/year per °C. When applied to future warming scenarios of the Intergovernmental Panel on Climate Change, this relationship results in a projected sea-level rise in 2100 of 0.5 to 1.4 meters above the 1990 level.

Understanding global sea-level changes is a difficult physical problem, because complex mechanisms with different time scales play a role (1), including thermal expansion of water due to the uptake and penetration of heat into the oceans, input of water into the ocean from glaciers and ice sheets, and changed water storage on land. Ice sheets have the largest potential effect, because their complete melting would result in a global sea-level rise of about 70 m. Yet their dynamics are poorly understood, and the key processes that control the response of ice flow to a warming climate are not included in current ice sheet models [for example, meltwater lubrication of the ice sheet bed (2) or increased ice stream flow after the removal of buttressing ice shelves (3)]. Large uncertainties exist even in the projection of thermal expansion, and estimates of the total volume of ice in mountain glaciers and ice caps that are remote from the continental ice sheets are uncertain by a factor of two (4). Finally, there are as yet no

published physically based projections of ice loss from glaciers and ice caps fringing Greenland and Antarctica.

For this reason, our capability for calculating future sea-level changes in response to a given surface warming scenario with present physics-based models is very limited, and models are not able to fully reproduce the sea-level rise of recent decades. Rates of sea-level rise calculated with climate and ice sheet models are generally lower than observed rates. Since 1990, observed sea level has followed the uppermost uncertainty limit of the Intergovernmental Panel on Climate Change (IPCC) Third Assessment Report (TAR), which was constructed by assuming the highest emission scenario combined with the highest climate sensitivity and adding an ad hoc amount of sea-level rise for “ice sheet uncertainty” (1).

While process-based physical models of sea-level rise are not yet mature, semi-empirical models can provide a pragmatic alternative to estimate the sea-level response. This is also the approach taken for predicting tides along coasts (for example, the well-known tide tables), where the driver (tidal forces) is known, but the calcula-

tion of the sea-level response from first principles is so complex that semi-empirical relationships perform better. Likewise, with current and future sea-level rise, the driver is known [global warming (1)], but the computation of the link between the driver and the response from first principles remains elusive. Here, we will explore a semi-empirical method for estimating sea-level rise.

As a driver, we will use the global average near-surface air temperature, which is the standard diagnostic used to describe global warming. Figure 1 shows a schematic response to a step-function increase in temperature, after climate and sea level parameters were at equilibrium. We expect sea level to rise as the ocean takes up heat and ice starts to melt, until (asymptotically) a new equilibrium sea level is reached. Paleoclimatic data suggest that changes in the final equilibrium level may be very large: Sea level at the Last Glacial Maximum, about 20,000 years ago, was 120 m lower than the current level, whereas global mean temperature was 4° to 7°C lower (5, 6). Three million years ago, during the Pliocene, the average climate was about 2° to 3°C warmer and sea level was

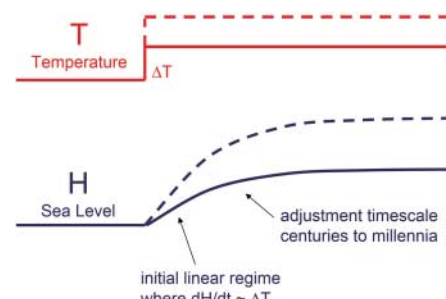


Fig. 1. Schematic of the response of sea level to a temperature change. The solid line and the dashed line indicate two examples with different amplitude of temperature change.

Potsdam Institute for Climate Impact Research, 14473 Potsdam, Germany. E-mail: rahmstorf@ozean-klima.de